CO adsorption on pure, defective and mixed composition AlF3 and MgF2 surfaces

Anthony Impellizzeri, Julien Dieu, Julie Rousseau, Sylvette Brunet, Christopher Ewels

ARTICLE

CO adsorption on pure, defective and mixed composition AlF_3 and MgF_2 surfaces

Full version in Catalyst Science and Technology
Accepted 24th April 2024
DOI

https://doi.org/10.1039/D4CY00174E

A. Impellizzeri [a]*, J. Dieu[b]*, J. Rousseau[b], S. Brunet[b]†, C. P. Ewels[a]†

AlF_3 and MgF_2 are important catalysts for fluorination processes. In this study we characterise structures consisting of either AlF_3, or MgF_2 supported over AlF_3, using Fourier Transform Infrared Spectroscopy of surface absorbed CO. We intepret the results using atomic-scale density functional calculations, along with high-resolution electron microscopy and spectroscopy. By coupling theory to vibrational spectroscopy we are able to establish different stable facets in the host species, identifying both surface physisorbed CO binding to pristine facets, and chemisorbed CO binding to fluorine anion vacancy sites. In the case of MgF_2 supported over AlF_3 surfaces we suggest that a 50:50 mixed Mg-AlF_x monolayer surface phase can form. Excess MgF_2 deposition subsequently results in the formation of MgF_2 nanoparticles on the surface. Mixed composition surface phases may play a critical role in Al/MgF_x fluorine catalysis.

Introduction

In heterogeneous catalysis, catalyzed fluorination of chlorinated molecules as starting materials involves Cl/F exchange, with HF as a fluorinating agent and metal fluorides as catalysts. Depending on the reactivity of chlorinated molecules, typically either bulk metal fluoride catalysts are used, or metal fluorides supported on an aluminium fluoride scaffold (AlF_3). For example, chromium oxyfluoride doped with zinc, magnesium or nickel supported on aluminium fluoride is commonly used for the fluorination of chlorinated aliphatic molecules[1,2]. On the other hand, bulk magnesium fluoride (MgF_2) catalysts appear to be the most active for the transformation of chlorinated aromatics such as 2-chloropyridine[3,4]. In all cases, the main difficulty is to have stable catalysts under HF gas flow with the largest possible specific surface area. This is the justification for the use of a support such as AlF_3. Maximising the surface area also allows better accessibility to the catalytically active sites, composed of metal atoms with unsaturated coordination and Lewis acidity properties.

Cl/F exchange reactions occur in very harsh environments, and as such it is extremely difficult to determine the *in-situ* surface chemistry of the catalysts. The *ex-situ* catalytic properties of the active sites of can be characterized via infrared vibrational spectroscopy of probe molecules such as carbon monoxide (CO). For example, by CO Fourier Transform Infrared Spectroscopy (CO-FTIR), a relationship between the amount of CO adsorbed and the adsorption strength of CO was established for the transformation of 2-chloropyridine[3,4].

An important tool to explore catalytic surface behaviour is atomic-scale modelling, notably via density functional theory (DFT)[5–13]. DFT has been used to explore the energetics of surface faceting in AlF_3 [9,13,14] and MgF_2 [5–7,10–12], as well as surfaces with vacant fluorine sites[5,8]. There are also some literature DFT studies of surface gas adsorption, including NH_3 on AlF_3 [9], and CH_4 [15] and CO [10] on MgF_2.

Despite this extensive modelling effort there rest many open questions. There is a lack of consensus in the literature concerning the energetic ordering of stable facets of MgF_2 [6,7,10,11]; there is general agreement that the (111) surface is unstable but the energetic ordering of the (110), (100) and (101) surfaces varies. X-ray diffraction suggests the $(01\bar{1}2)$ oriented surface of α-AlF_3 is the most exposed[16], but the surface structure remains open with both non-reconstructed[14,16] and a more stable $\sqrt{2} \times \sqrt{2}$ reconstructed[9] $(01\bar{1}2)$ surface models proposed (and others finding $(01\bar{1}0)$ more stable[14]). There is no literature that we are aware of exploring mixed composition surfaces. Furthermore, there are not yet any consistent studies exploring CO adsorption on both pristine and defective materials.

In this current work, using consistent levels of theory, we explore both MgF_2 and AlF_3 surfaces, their surface vacancies, and absorption behaviour of CO on pristine and defective surfaces. This allows accurate correlation to new experimental FTIR data and classify the observed FTIR peaks. From this, we propose the existence of a new mixed $Al_{0.5}Mg_{0.5}F_x$ monolayer surface phase coating AlF_3, which appears highly catalytically active.

Method

Synthesis

Commercial alumina was fluorinated using HF at 400°C to obtain a partially fluorinated support, which was stabilized under fluorination conditions[17] with a specific surface area of around 63 m^2/g. Mg catalysts supported over partially fluorinated alumina (55 wt% AlF_3) were prepared by wetness impregnation of the fluorinated alumina with an aqueous solution of magnesium nitrate, in order to obtain 2-6 wt% Mg deposition. AlF_3 impregnation was carried out at room temperature and atmospheric pressure. The catalysts were then dried at 110 °C for one night under atmospheric pressure. Precursors were decomposed at 380°C and atmospheric pressure under nitrogen flow. These samples were also treated under HF gas diluted in nitrogen (HF/N_2 molar = 4) at 350°C for 2 hours at atmospheric pressure. This treatment lowers the specific surface area to 37 m^2/g, but ensures that any residual surface hydroxyl is removed and surface layers are fully fluorinated, confirmed with XPS.

Characterisation

Elemental analysis of Mg was determined by inductively coupled plasma-optical emission spectrometry (ICP-OES) using a PerkinElmer Optima 2000DV instrument. Mg/AlF_3 sample morphology was evaluated by Transmission Electronic Microscopy (TEM) using a JEOL JEM2100LAB6 (JEOL, Tokyo, Japan) equipped with an EDX JED JEOL, operating at 200kV (10nm beam spot size). Samples were dispersed in ethanol then deposited directly onto a Cu MET lacey carbon grid. X-ray diffraction (XRD) shows that samples maintain a good degree of crystallinity, although peak assignment is complex due to the mixture of phases present (see Supplementary Materials, Figur S5).

Specific surface areas (BET method) of materials were measured by nitrogen-physisorption at −196°C (TRISTAR 3000) after treatment at 250°C for 2h. The amount and strength of Lewis acidity of the coordinatively unsaturated sites (CUS) was determined by CO adsorption followed by transmission FTIR spectroscopy[3,4]. Spectra were recorded over a 1000-4000 cm^{-1} range using a ThermoNicolet NEXUS 5700 spectrometer with a resolution of 2 cm^{-1}. 64 scans per spectrum were collected. Samples were pressed into thin 16mm diameter pellets (10-60 mg, specific surface area of $2cm^2$, applied pressure of 1 to 2 $tonnes.cm^{-2}$) and placed in an IR cell fitted with quartz or CaF_2 window. They are activated *in-situ* for one night at 300°C under nitrogen (~100mL/min). After unaided cooling to room temperature, the cell was further cooled to 100 K with liquid nitrogen. A background spectrum was collected which was then subtracted from the other spectra obtained after CO adsorption. Successive doses of CO were then introduced from a given volume (V=0.4125 cm^3) subjected to a known CO pressure (from 5 to 200 mbar) until saturation, obtained by subjecting the samples to a CO pressure of 1 mbar at equilibrium. After each dose of CO is introduced an IR spectrum is taken, until saturation is reached. The final spectrum was recorded with 1 Torr of CO at equilibrium pressure (saturation). All spectra are normalized to an equivalent sample mass (25 mg). The amount of Lewis acid sites are quantified by integrating the total area of the IR bands at saturation between 2100 and 2200 cm^{-1}.

Transformation of 2-chloropyridine

The fluorination of 2-chloropyridine (2ClPy) was carried out at 350°C under atmospheric pressure in a fixed bed reactor in a dynamic flow during 4 h 30 min[3,4]. The catalyst was first activated in situ by HF diluted in nitrogen (N_2/HF: 1/4) for 1 h at 350°C (activation step). 2-chloropyridine was then injected into the reactor using a syringe pump. The organic gas products were trapped in 1,2-dichloroethane. HF and HCl were quenched in water at the outlet of the reactor. The organic components were analyzed with a Scion 456 gas-phase chromatograph (Bruker) equipped with a DB5 capillary column (inside diameter of 0.2 mm, film thickness of 1 mm, length 30 m). The oven temperature was raised from 100 to 200°C at 5°C min^{-1}.

The catalytic activity ($mmol.h^{-1}.g^{-1}$) is defined as the conversion of 2-chloropyridine multiplied by the flow of the chlorinated substrate, divided by the mass of catalyst. Only 2-fluoropyridine (2FPy) and HCl were observed as reaction products. Thus, the selectivity towards 2-fluoropyridine was equal to 100% and the conversion of 2-chloropyridine corresponded to the 2-fluoropyridine yield. In these experiments, the molar balance was always higher than 90%. No thermal conversion of 2-chloropyridine was observed.

Computational Method

DFT calculations were performed with the AIMPRO code[18–20] under both the local density approximation (LDA) and generalized gradient approximation (GGA) parametrized by Perdew, Burke, and Ernzerholf (PBE)[21]. Van der Waals forces are treated using different Grimme's dispersion correction: D2[22], D3[23], and D3 with Becke-Johnson (BJ) damping[24]. Relativistic pseudopotentials are included via the Hartwigsen-Goedecker-Hütter scheme[25]. The wavefunction basis consists of Gaussian function sets multiplied by polynomial functions including all angular momenta up to maxima d (l = 0-2). All elements involved in this study (Mg, F, C, O, and Al) are described using a large *dddd* basis set with 40 independent functions per atom, except hydrogen in HF and FHF^- which is described with *ppp*, i.e. 12 independent functions. A non-zero electron temperature of kT = 0.02 eV for electronic level occupation was taken using a Fermi smearing function to facilitate convergence, with a high plane wave energy cutoff (350 Ha). Our choice of exchange-correlation functionals and van der Waals corrections are justified by comparative calculations for bulk MgF_2 and AlF_3, and vibrational response of gas-phase CO and CO_2 (see Supplementary Materials Table S1).

Tetragonal unit cell are used for the MgF_2 bulk structure with space group P_{42}/mnm. Cells were optimized using a 12×12×12 k-point grid (tested for convergence), until maximum atomic position change in a given iteration drops below 10^{-6} a_0 (a_0: Bohr radius) and total energy was converged to within a

tolerance of 10^{-7} Ha (Ha: Hartree energy). Built from the optimized bulk structure, we modelled slabs in orthorhombic cells with thickness between 3.09—21.66 Å (12-48 atoms). (110), (100), (101), and (001) facets have been considered. Atom positions and in-plane lattice vectors are fully relaxed with no symmetry constraints with $n \times m \times 1$ k-points chosen to maintain uniform k-point density and depending on the length of each in-plane lattice vector (convergence with k-points is demonstrated further in Supplementary Materials Table S2). In the out-of-plane direction, cell sizes are large enough (~20 Å between slabs) to avoid interaction. Surface energies are calculated by subtraction of total energy from equivalent bulk system.

Orthorhombic α-AlF_3 slabs were constructed in a similar way, including (0001) and (10$\bar{1}$1) orientations, as well as (01$\bar{1}$2) in both the unreconstructed and $\sqrt{2} \times \sqrt{2}$ reconstructions.

Once the slabs are optimised, a CO molecule is added above the surface in different positions and orientations. The molecule and neighbouring surface layer are relaxed with the rest of the slab and periodic lattice vectors held fixed.

Charge transfer is evaluated using Mulliken population analysis. Electronic properties have been determined using 24×24×24 and 48×48×1 k-point grids for bulk and slab configurations, respectively. For the projected density of states calculations, energy broadening was set to 0.04 eV.

CO vibrational frequencies are calculated by determining the energies and forces for 0.11 Å displacements of atoms in the adsorbed molecule. The second derivatives of the energy with respect to the positions of atoms are then obtained by a finite difference formulation, leading directly to the dynamical matrix. Frequency calculations require a high level of precision, and for this reason we increase the energy tolerance for the self-consistent calculation from 10^{-7} Ha to 10^{-10} Ha. We have investigated the effect of slab thickness on CO frequencies, showing that even for the thinner slabs the system is already well converged, with variation in the CO frequency with slab thickness of only ±1-3cm^{-1} (see Supplementary Materials Figures S1, S2 and Tables S3, S4).

Results and Discussion

Calculated Surfaces Energies for MgF_2 and α-AlF_3

	Calculated Surface Energy (J/m^2)
α-AlF_3	
(01$\bar{1}$2) $\sqrt{2} \times \sqrt{2}$	**1.21**
(01$\bar{1}$2) unreconstructed	1.41
(01$\bar{1}$0) unreconstructed	1.27
MgF_2	
(110) unreconstructed	**0.90**
(100)/(010) unreconstructed	1.00
(011)/(101) unreconstructed	1.00
(001) unreconstructed	1.25
α-AlF_3 with surface monolayer of $Al_{0.5}Mg_{0.5}F_3$	
(01$\bar{1}$2) unreconstructed diagonal Al	**0.98**
(01$\bar{1}$2) unreconstructed straight Al	1.08
(01$\bar{1}$2) reconstructed without external F	1.00

Table 1: Calculated surface energies (J/m^2) for key stable AlF_3 and MgF_2 facets. The surface energy of the mixed species is lower than the average of the two isolated surfaces, i.e. there is a thermodynamic driving force for a mixed surface phase rather than segregation.

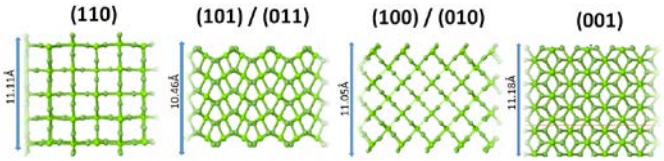

Figure 1 Cross-section through infinite periodic 2D slabs of MgF_2 with different surface crystallographic orientation. Slab thicknesses in Angstroms, stability decreases from left to right (see Table 1). Slab surface is at the top and bottom of each figure.

Calculated surface energies for MgF_2 and α-AlF_3 are given in Table **1**. The MgF_2 (111) facet is extremely unstable and not included here. Facet stability order is consistent with Han *et al* [5], i.e. for MgF_2 (110) < (101)/(011) < (100)/(010) < (001) < (111). The stable (110) surface consists of lines of truncated octahedral with exposed 5-fold coordinated Mg, interspersed with protruding lines of fluorine atoms, each bound to two underlying Mg. The (101) facet is very close in energy and consists of ridges lined with 5-fold coordinated Mg and fluorine at the ridge tops.

For AlF_3 we focus on the hexagonal α-AlF_3 phase as the most thermodynamically stable, which has octahedrally coordinated F atoms around each Al. In the literature the (01$\bar{1}$2) surface was found to be significantly more stable due to a $\sqrt{2} \times \sqrt{2}$ surface reconstruction (0.76 Jm^{-2}), followed by ($\bar{2}$110) (1.04 Jm^{-2}) and then (0001)/(10$\bar{1}$1) (1.15 Jm^{-2})[9,13]. However a more recent study of unreconstructed facets and charge states found (01$\bar{1}$0) most stable (1.01 Jm^{-2}), followed by (11$\bar{2}$0) (1.05 Jm^{-2})[14]. Consistent with both earlier studies, we find the (01$\bar{1}$2) $\sqrt{2} \times \sqrt{2}$ reconstruction the most stable, with the unreconstructed (01$\bar{1}$2) less stable than (01$\bar{1}$0). AlF_3 atomic surface structures can be seen in Figure 4.

CO absorption on pristine and defective AlF_3 surfaces

Details of frequency calculations for isolated gas phase CO and CO_2 are given in Supplementary Materials (Figures S1, S2 and Tables S3, S4). We take the difference between our calculated CO stretch frequency and the experimental value as an offset that we apply to all calculations hereafter for CO bound to surfaces.

Our experimental FTIR data for CO absorption on AlF_3 is given in Figure 2. Three CO-related peaks can be seen, one very broad centred at ~2162cm^{-1}(+19cm^{-1} over gas phase CO), and two sharper overlapping peaks at 2227.6cm^{-1} (+84.6cm^{-1}) and 2233.2cm^{-1} (+90.2cm^{-1}, appearing as a shoulder on the first). The lower frequency and broadness of the 2162 cm^{-1} peak suggests weakly bound CO without significant site selectivity, whereas the 2227.6 and 2233.2cm^{-1} peaks, being sharper and higher energy suggest stronger binding to more localised and specific sites. There is additionally always two CO_2 peaks visible.

This is reminiscent of literature data for high-surface AlF_3 (HS-AlF_3) where modes are seen at 2150, 2170, 2220 and 2240 cm^{-1}, [26] and milled α-AlF_3 with peaks at 2150, 2170 and 2220cm^{-1}.[27] In the literature cases the 2150-2170 cm^{-1} peaks are however much sharper and more intense.

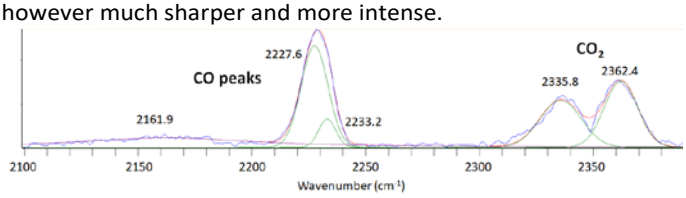

Figure 2 Experimental FTIR spectrum for CO absorption on AlF_3. Frequency in wavenumbers (cm^{-1}).

We have calculated the structure, binding and associated stretch frequency for CO on both pristine α-AlF_3 facets, and surfaces with a single positive fluorine vacancy (i.e. removal of F^-), focussing on the $\sqrt{2} \times \sqrt{2}$ reconstructed (01$\bar{1}$2) surface as the thermodynamically most stable.

CO on the unreconstructed (01$\bar{1}$2) surface shows a +48cm^{-1} frequency upshift (2185 cm^{-1} in our calculations), and is most stable with the C closest to the 5-fold coordinated surface Al (Figure 3a). On the $\sqrt{2} \times \sqrt{2}$ reconstructed (01$\bar{1}$2) surface this shifts to 2166.8 cm^{-1} (+31cm^{-1}), with CO bonding again to a 5-fold coordinated Al, forcing the top F atom off-site to accommodate the CO (Figure 3b). On the (01$\bar{1}$0) facet, the CO aligns with C facing a 4-fold coordinated surface Al, with calculated CO stretch frequency of 2167 cm^{-1} (+31 cm^{-1} upshift) (see Figure 3c).

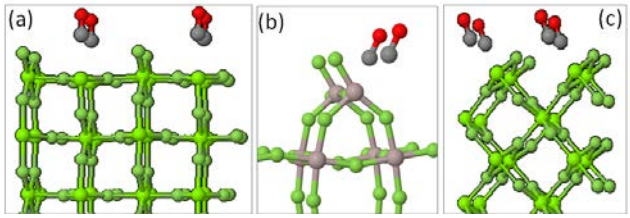

Figure 3 CO physisorption sites on the (a) unreconstructed (11$\bar{2}$0), (b) reconstructed (11$\bar{2}$0) and (c) (10$\bar{1}$1) surfaces of α-AlF_3. The CO stretch frequency shows an upshift of (a) 48 cm^{-1} and (b,c) 31cm^{-1} compared to gas phase.

Previous theoretical modelling[28] also explored CO binding to pristine α-AlF_3 and found similar values to us for the (01$\bar{1}$0) surface (2165 cm^{-1}), and higher values of 2190-2205 cm^{-1} for the unreconstructed (11$\bar{2}$0). For the (11$\bar{2}$2) surface (not considered here), they obtained 2187 cm^{-1} on the tetrahedral site and 2158 cm^{-1} on the five-fold coordinated site.

On the basis of our theoretical, experimental and literature data, we conclude that the broad lower peak seen in experiment around 2160 cm^{-1} is due to physisorbed CO on AlF_3 surfaces, most likely reconstructed (11$\bar{2}$0) and (01$\bar{1}$0), although the broadness of this peak suggests our sample is not highly crystalline. Since the spectra are normalised it is also possible that we have a very high concentration of surface defects (see next section) which results in the higher wavenumber peaks dominating the spectra.

It appears that physisorption cannot explain the observed higher frequency CO FTIR peaks above 2200cm^{-1} in Figure 2. We therefore next explore the binding behaviour of CO to point defects, the most common of which will be surface F^- vacancies.

We consider removal of singly coordinated F anions, present on both the reconstructed and unreconstructed (01$\bar{1}$2) surfaces (see Figure 4). CO chemisorbs directly to the exposed Al, resulting in upshifted stretch frequencies compared to the physisorbed situation discussed above. On the unreconstructed (01$\bar{1}$2) surface we find CO stretch frequencies of 2231 cm^{-1} (+94 cm^{-1}), rising to 2256.1 cm^{-1} (+119 cm^{-1}) on the reconstructed surface. Binding to the other exposed Al on the unreconstructed surface gives CO frequency of 2218.1 cm^{-1} (+81.1 cm^{-1}).

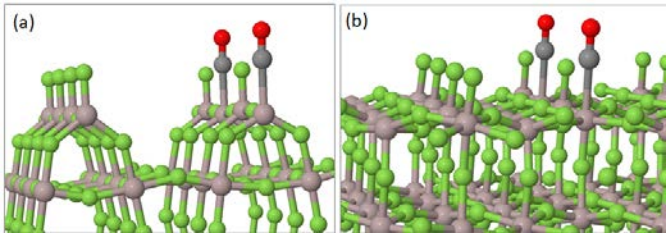

Figure 4 CO chemisorption on F^- surface vacancy sites of (a) reconstructed and (b) unreconstructed (01$\bar{1}$2) AlF_3. The CO stretch frequency shows an upshift of (a) 119 cm^{-1} and (b) 94 cm^{-1} compared to gas phase.

There is also an unstable cutting plane of the (01$\bar{1}$0) surface giving singly-coordinated F sites; in this case replacing F^- with CO results in a structure similar to Figure 3c with this time a CO stretch frequency of 2249.1 cm^{-1} (+112 cm^{-1}).

The best agreement between theory and experiment comes from the unreconstructed (01$\bar{1}$2), where the underlying Al atom was at the centre of an octahedron but is now five-fold coordinated. Where CO binds to four-fold coordinated Al (e.g. beneath the F^- vacancy on reconstructed (01$\bar{1}$2)) the calculated CO frequency is too high compared to experiment.

Several other factors with affect the CO frequency, including notably surface site density, as discussed by Huesges *et al*[10]. Equally surface charge plays a role; if we take CO physisorbed to the vacancy-free $\sqrt{2} \times \sqrt{2}$ reconstructed (01$\bar{1}$2) surface, simply adding a +1 charge to the system shifts the CO frequency from 2166.8 cm^{-1} to 2193.4 cm^{-1} (an upshift of 26.6cm^{-1}).

Given these considerations, precise defect assignment for these experimental peaks is difficult, particularly as the experimental sample is not highly crystalline. Additionally, within the experimental peak fit there are small variations in the fitting of the peak tail, suggesting there may be further low-intensity peaks within the overall curve in this frequency range. There is also significant variation in these and literature frequencies for AlF_3 in this range.[26,27]

The calculations are nonetheless in the correct frequency range and we can assign these two sharp experimental peaks to CO bound to two distinct types of vacant F^- site on the AlF_3 surface.

CO adsorption on pristine and defective MgF_2 surfaces

We next explore CO on pristine MgF_2 surfaces (see Figure 5). As for AlF_3, the most stable configurations are with C facing the surface in proximity to a metal cation, with the CO frequency upshifted in the range 2173-2189 cm^{-1}. On the (001) facet, the CO frequency is 2173 cm^{-1} (+36 cm^{-1}). On the most stable (110) surface this increases to 2189 cm^{-1} (+52 cm^{-1}), while on the (101)/(011) it is 2162cm^{-1} (+25 cm^{-1}) and for the (100) is it 2168 cm^{-1} (+31 cm^{-1}). The most stable configuration on the (110) surface corresponds to sitting above Mg completing its truncated octahedron coordination, i.e. binding to a 5-fold coordinated Mg.

Although we quote here the most stable binding site, on many of these surfaces the energy to translate CO across the surface can be very small. This is indicative of weak physisorption behaviour and suggests the CO will be surface mobile. The full range of calculated structures, energies and associated frequencies are given in Supplementary Materials (Figure S3).

Our calculated values are in good agreement with Huesges et al[10] who found shifts of +57 cm^{-1} for (110), +53 cm^{-1} (101) and +39 cm^{-1} for (001). The difference with our value for the (101) surface we ascribe to CO surface density, since they found that increasing CO surface density drops this shift to only +27cm^{-1}.

We note that for the most stable surfaces in each case, CO physisorbed on MgF_2 has a calculated stretch frequency around 20 cm^{-1} higher than on AlF_3.

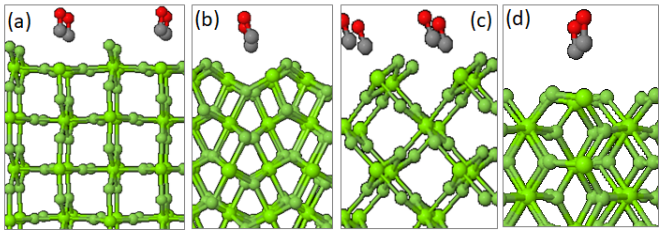

Figure 5 CO physisorption sites on the (a) (110), (b) (101) / (011), (c) (100) and (d) (001) surfaces of MgF_2. The CO stretch frequency shows an upshift of (a) 52 cm^{-1} (b) 25 cm^{-1}, (c) 31 cm^{-1} and (d) 36 cm^{-1} compared to gas phase.

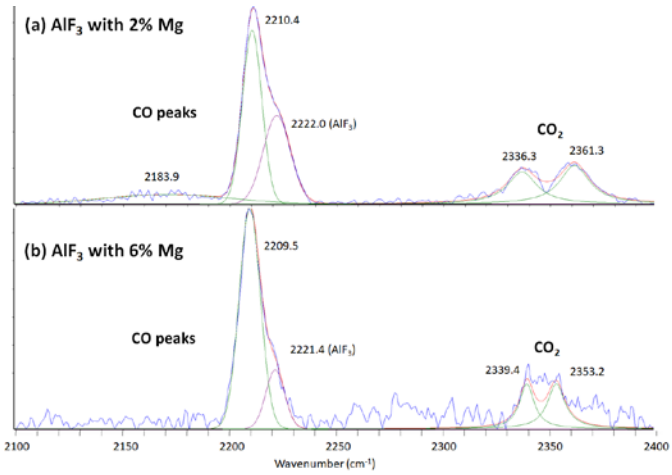

Figure 6 Experimental FTIR spectrum for CO absorption on AlF_3 doped with (a) 2 wt% and (b) 6 wt% Mg. Frequency in wavenumbers (cm^{-1}).

We next add MgF_2 to AlF_3 via impregnation of the fluorinated alumina with an aqueous solution of magnesium nitrate. The resultant FTIR spectra show a number of modified and new features as compared to the pristine AlF_3 case (Figure 6). The broad low frequency physisorption peak shows an upshift of around 20 cm^{-1}. While this peak is now so broad that quantitative comparison between theory and experiment cannot be justified, this is nonetheless consistent with the upshifts seen in our calculated CO frequencies when physisorbed on AlF_3 and MgF_2 surfaces respectively.

The major change in the FTIR spectra is the appearance of a strong peak at 2210 cm^{-1} (+67 cm^{-1}). Increasing Mg concentration both strengthens this new peak and suppresses the AlF_3 defect peak at 2222 cm^{-1}, suggesting that this new feature occurs at the expense of that associated with AlF_3 defects. This peak is also slightly sharper (width of 10.7 cm^{-1} compared to 15.0 cm^{-1} for the 2222cm^{-1} AlF_3 peak), suggesting a more uniform local structure.

Turning again to the calculations, adding CO to F^- vacancy sites on MgF_2 leads to calculated frequency upshifts similar to those seen with AlF_3. Binding CO to a bidentate F^- vacancy on the (110) MgF_2 facet gives a CO frequency of 2209 cm^{-1} (+72 cm^{-1}), while on the unstable (001) facet the CO frequency rises from 2173 to 2202 cm^{-1}, i.e. +65 cm^{-1} compared to gas-phase CO. Thus an initial assessment would suggest assigning this new peak to F^- vacancy sites on MgF_2.

A simple picture of Mg catalyst on AlF_3 scaffolding would be the formation and activity of catalytic MgF_2 nanoparticles on an inactive AlF_3 surface. Examining the two Mg treated samples via TEM (Figure 7), we can indeed see MgF_2 particle presence at higher Mg concentration (Points 4, 5 in Figure 7c). However, the lower concentration (2 wt% Mg) samples show relatively uniform Mg distribution without the presence of Mg-rich nanoparticles.

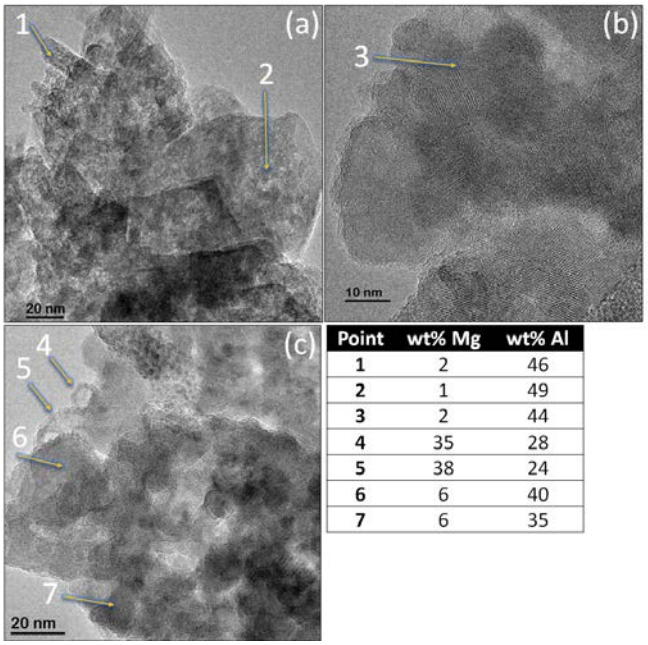

Point	wt% Mg	wt% Al
1	2	46
2	1	49
3	2	44
4	35	28
5	38	24
6	6	40
7	6	35

Figure 7 Representative Transmission Electron Microscopy images of (a,b) 2wt% and (c) 6wt% Mg treated AlF_3 after HF activation. Scale bars are given on each image. Energy dispersed x-ray (EDX) analysis was performed at the numbered and arrow-marked points, with the Mg and Al concentration measured at each point given in the Table. The untreated AlF_3 scaffolding is shown in Supplementary Materials Figure S4 for reference.

The picture of MgF_2 nanoparticle deposition on a support structure is also not consistent with the observed FTIR. Specifically, the suppression of the existing AlF_3 defect signal suggests the Mg is not simply using AlF_3 as a support but is instead modifying its surface.

If distributed in a continuous monolayer, 2 wt% Mg could theoretically cover ~50% of the measured BET surface area of the AlF_3 support ($62m^2/g$), rising to ~100% coverage for the HF treated surface ($37m^2/g$). 6 wt% Mg is then in excess of the theoretical monolayer coverage. A model with MgF_2 wetting the AlF_3 surface, and excess Mg forming MgF_2 nanoparticles, is consistent with the above experimental observations. Indeed it has been proposed previously that monolayer metal surface wetting may occur in fluoride catalysts[2] but no atomic structure models have been proposed to date.

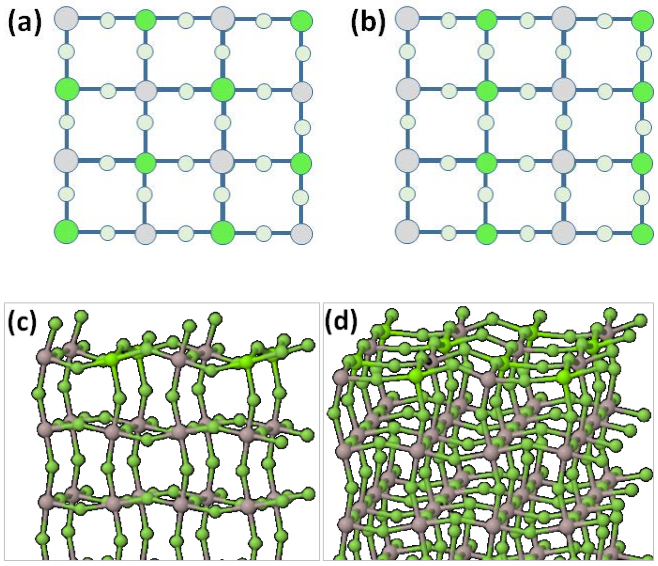

Figure 8 (a,b) Schematic showing top-down view of 50:50 mixed Mg-Al fluoride monolayer structures on the unreconstructed (01$\bar{1}$2) AlF_3 surface. Fluorine atoms are small circles, Mg large green and Al large grey. Calculated surface energies are given in Table 1. Structure (a) alternating "chess board" configuration has the lowest formation energy and is more stable than segregated (110) MgF_2 and (01$\bar{1}$2) AlF_3 surfaces. (c,d) Side-view of atomic structure of this surface (c) with and (d) without surface monodentate fluorine on the Al. Structure (d) is the stable surface.

We have explored the structural stability of 50% composition Al-Mg surfaces, by substituting half the surface Al sites in the (01$\bar{1}$2) non-reconstructed AlF_3 cells with Mg. We consider alternating Al and Mg in both ("chess board" structure, Figure 7a) and just one (linear structure, Figure 7b) surface directions. The calculated surface energies are given in Table 1, showing that the chess-board structure is extremely stable at only 0.98 J/m^2. Not only is it significantly more stable than the pristine $\sqrt{2} \times \sqrt{2}$ reconstructed (01$\bar{1}$2) AlF_3 surface (1.21 J/m^2), it is also more stable than the average of the $\sqrt{2} \times \sqrt{2}$ (01$\bar{1}$2) AlF_3 and (110) MgF_2 surfaces (1.06 J/m^2). This suggests that there will be a strong thermodynamic driving force for formation of a mixed surface phase rather than segregation. Indeed, a non-reconstructed (01$\bar{1}$2) AlF_3 cell where the surface is segregated into two zones, each with three rows of either Mg or Al, has a surface energy 0.45J/m^2 less stable than the alternating chess-board surface.

We suggest therefore that experimentally, upon introduction of Mg to the AlF_3 support, the first step is formation of a mixed AlMg surface phase over the AlF_3. Once this forms a monolayer, further Mg addition leads to the formation of MgF_2 nanoparticles on the scaffold surface.

Unlike the AlF_3 surface which has monodentate fluorine attached to the Al, the 50:50 Mg:Al surface is most stable without them. The calculated binding energy of F^- to the 50:50 Mg:Al surface (converting Figure 7d to Figure 7c) is 2.68eV/F^- less than the equivalent process for a pure AlF_3 surface. Thus for example, creating gas phase FHF^- from gas phase HF and a surface monodentate F^- is strongly endothermic using the AlF_3 surface (+2.30eV), but weakly exothermic from a AlMg surface (Figure 7c) (-0.38eV). This is consistent with the close calculated surface energies with and without monodentate surface F for the mixed surfaces (0.98 J/m^2 and 1.00 J/m^2 respectively, see Table 1).

This suggests that F addition and removal to the mixed surface will be extremely easy. Thus such a mixed-phase surface is likely to be catalytically active due to the variety of different charge states exposed on the surface, and the ease with which the surface can capture and release F atoms.

To explore this further we tested the catalytic performance for the fluorination transformation of 2-chloropyridine. Catalysis was performed at 350°C, with gas mixture ratio of HF/N_2/2-chloropyridine of 6:1.7:1. The catalytic activity is reported in Table 2. Cl/F exchange is very fast, and for all catalysts the activity is stable only after 2 hours. It can be seen that although the specific surface area remains roughly constant after Mg treatment, the catalytic activity of the AlF_3 is increased by a factor of 5-6. Importantly, the 2 wt% and 6 wt% Mg samples show the same catalytic activity (around 10 mmol.h^{-1}.g^{-1}) despite the absence of MgF_2 nanoparticles in the 2 wt% Mg case, suggesting the catalytic activity is not linked to the MgF_2 nanoparticles. This is consistent with our surface layer model.

Catalyst	S_{BET} (m^{2}g^{-1})	Activity (mmolh^{-1}g^{-1})
AlF_3	37	2
Mg 2%wt / AlF_3	25	11
Mg 6%wt / AlF_3	35	10

Table 2: Catalytic activity for transformation of 2-chloropyridine by AlF_3 and Mg-treated AlF_3. Specific surface area (S_{BET}) is given in m^{2}g^{-1}, catalytic activity in mmolh^{-1}g^{-1}.We note that the calculations alone cannot exclude the possibility of further MgF_2 deposition on the 50:50 monolayer surface. Such a layer could be consistent with our calculated CO IR frequencies for adsorption on F^- vacancies on MgF_2, which show peak shifts close to the experimental 2210 cm^{-1} peak. Further high-resolution surface TEM would be necessary to distinguish this, which is beyond the scope of the current study.

Summary and Conclusions

DFT calculations exploring the stability of different surface facets in MgF_2 and AlF_3 are consistent with much of the prior literature. Facet stability order for MgF_2 is consistent with Han *et al* [5], i.e. the most stable facet is (110) < (101)/(011) < (100)/(010) < (001) < (111). For α-AlF_3, our calculations agree with Bailey *et al*,[9,13] finding the (01$\bar{1}$2) $\sqrt{2} \times \sqrt{2}$ reconstruction the most stable, with the unreconstructed (01$\bar{1}$2) less stable than (01$\bar{1}$0).

FTIR measurements for CO surface absorption on AlF_3 and Mg-decorated AlF_3 show a range of peaks, with broad peaks in the 2100-2200cm^{-1} range corresponding to surface physisorption of CO, and higher frequency peaks from 2200-2240cm^{-1} corresponding to chemisorbed CO at charged surface vacancies on AlF_3.

Addition of Mg results first in the creation of a novel mixed AlMg monolayer phase on the unreconstructed (01$\bar{1}$2) surface of AlF_3, before excess MgF_2 then forms surface nanoparticles. The surface consists of alternating Al and Mg in a checkerboard pattern, separated with bidentate fluorine. Our results suggest that this mixed 50:50 Al:Mg surface is catalytically active, showing relative facility for removal/addition of fluorine and charge. Indeed it appears that this monolayer mixed phase is

responsible for the catalytic behaviour of the hybrid system rather than the MgF_2 nanoparticles also present.

As far as we are aware, Mg is not soluble in bulk AlF_3. There are no bulk $Mg_xAl_{1-x}F_y$ phases recorded in the ICSD database[29], and the only computationally predicted phase to date[30], $MgAlF_5$, is predicted to be unstable with respect to MgF_2 and AlF_3. On surface facets however, the symmetry breaking, and possibilities for charge redistribution and elastic deformation open the possibility for the formation of stable monolayer surface phases, such as Al-Mg described here.

This suggests it might be useful to explore other metallic alloy monolayer coverage on metallic fluorides as an efficient and low concentration route to producing active catalytic surfaces.

Author Contributions

C.E. and S.B. conceived the study, A.I. and C. E. performed and analysed the calculations, J.D. performed all experiments, J.B. performed TEM and EDX. C.E. analysed data and wrote first draft, all authors wrote and edited the article.

Conflicts of interest

There are no conflicts to declare.

Acknowledgements

This work received funding from the French Agence Nationale de Recherche Project ANR-20-CE08-0026 “OPIFCat”. A.I. and C.E. acknowledge the GLICiD regional mesocentre at Pays de la Loire where many of the calculations were performed. We thank V. Maisonneuve, the Solvay company (represented by Eric Périn and François Metz) and other colleagues in the OPIFCat project for useful scientific discussions.

1 H. Bozorgzadeh, E. Kemnitz, M. Nickkho-Amiry, T. Skapin and J. M. Winfield, *Journal of Fluorine Chemistry*, 2003, **121**, 83–92.

2 A. Loustaunau, R. Fayolle-Romelaer, S. Celerier, A. D’Huysser, L. Gengembre and S. Brunet, *Catal Lett*, 2010, **138**, 215–223.

3 A. Astruc, C. Cochon, S. Dessources, S. Célérier and S. Brunet, *Applied Catalysis A: General*, 2013, **453**, 20–27.

4 A. Astruc, S. Célérier, E. Pavon, A.-S. Mamede, L. Delevoye and S. Brunet, *Applied Catalysis B: Environmental*, 2017, **204**, 107–118.

5 H. Han, G. Yin, H. Wang, C. Wang, K. Shao, W. Zhang, J. Dai and P. Huai, *Computational Materials Science*, 2017, **133**, 159–166.

6 A. F. Vassilyeva, R. I. Eglitis, E. A. Kotomin and A. K. Dauletbekova, *Physica B: Condensed Matter*, 2010, **405**, 2125–2127.

7 A. Vassilyeva, R. Eglitis, E. Kotomin and A. Dauletbekova, *Open Physics*, 2011, **9**, 515–518.

8 A. F. Fix, F. U. Abuova, R. I. Eglitis, E. A. Kotomin and A. T. Akilbekov, *Phys. Scr.*, 2012, **86**, 035304.

9 C. L. Bailey, S. Mukhopadhyay, A. Wander, B. G. Searle and N. M. Harrison, *J. Phys. Chem. C*, 2009, **113**, 4976–4983.

10 Z. Huesges, C. Müller, B. Paulus, C. Hough, N. Harrison and E. Kemnitz, *Surface Science*, 2013, **609**, 73–77.

11 L.-L. ZHANG, P.-D. HAN, C.-L. ZHANG, M.-H. DONG, Y.-Q. YANG and X.-Y. GU, *Acta Physico-Chimica Sinica*, 2011, **27**, 1609–1614.

12 L. Hammerschmidt, L. Maschio, C. Müller and B. Paulus, *J. Chem. Theory Comput.*, 2015, **11**, 252–259.

13 C. L. Bailey, Imperial College London, 2009.

14 R. Pandharkar, C. Becker, J. H. Budau, Z. Kaawar and B. Paulus, *Inorganics*, 2018, **6**, 124.

15 A. Abbaspour Tamijani, *Computational and Theoretical Chemistry*, 2017, **1121**, 11–28.

16 S. Mukhopadhyay, C. L. Bailey, A. Wander, B. G. Searle, C. A. Muryn, S. L. M. Schroeder, R. Lindsay, N. Weiher and N. M. Harrison, *Surface Science*, 2007, **601**, 4433–4437.

17 Institut National de la Propriété Industrielle, Paris, FR2771027, 1999, 11.

18 M. J. Rayson and P. R. Briddon, *Computer Physics Communications*, 2008, **178**, 128–134.

19 M. J. Rayson and P. R. Briddon, *Phys. Rev. B*, 2009, **80**, 205104.

20 P. R. Briddon and M. J. Rayson, *physica status solidi (b)*, 2011, **248**, 1309–1318.

21 J. P. Perdew, K. Burke and M. Ernzerhof, *Phys. Rev. Lett.*, 1996, **77**, 3865–3868.

22 S. Grimme, *Journal of Computational Chemistry*, 2006, **27**, 1787–1799.

23 S. Grimme, J. Antony, S. Ehrlich and H. Krieg, *J. Chem. Phys.*, 2010, **132**, 154104.

24 S. Grimme, S. Ehrlich and L. Goerigk, *Journal of Computational Chemistry*, 2011, **32**, 1456–1465.

25 C. Hartwigsen, S. Goedecker and J. Hutter, *Phys. Rev. B*, 1998, **58**, 3641–3662.

26 Determination of the Acidity of High Surface AlF3 by IR Spectroscopy of Adsorbed CO Probe Molecules | The Journal of Physical Chemistry C, https://pubs.acs.org/doi/10.1021/jp075450t, (accessed 6 July 2023).

27 Mechanical Activation of α-AlF_3: Changes in Structure and Reactivity | Chemistry of Materials, https://pubs.acs.org/doi/10.1021/cm801135h, (accessed 6 July 2023).

28 C. Becker, T. Braun and B. Paulus, *Catalysts*, 2021, **11**, 565.

29 D. Zagorac, H. Müller, S. Ruehl, J. Zagorac and S. Rehme, *J Appl Cryst*, 2019, **52**, 918–925.

30 *Materials Data on $MgAlF_5$ by Materials Project*, Lawrence Berkeley National Lab. (LBNL), Berkeley, CA (United States). LBNL Materials Project, 2020.